PAPER

Check for updates

A new eco-friendly and highly emitting Mn-based hybrid perovskite toward high-performance green down-converted LEDs†

Asmae Ben Abdelhadi, [ID] [ab] Mario Gutiérrez, [ID] [a] Boiko Cohen, [ID] [a] Luis Lezama, [ID] [c] Mohammed Lachkar [ID] [b] and Abderrazak Douhal [ID] *[a]

As luminescent materials, lead-free zero-dimensional (0D) organic–inorganic metal halide perovskites have recently attracted special attention. Here, we have synthesized a novel lead-free manganese-based organic–inorganic hybrid halide $(TPA)_2MnBr_4$ where TPA = $[(C_3H_7)_3NH]^+$ (*i.e.*, tri-*n*-propyl-ammonium). The single crystal X-ray diffraction (SCXRD) shows that $(TPA)_2MnBr_4$ crystallizes in the triclinic phase and $P\bar{1}$ space group, with the lattice parameters of *a* = 9.5444(2) Å, *b* = 10.1056(2) Å and *c* = 15.1835(3) Å. The powder XRD (PXRD) pattern confirms the synthesized perovskite's high purity and crystalline nature. The crystalline structure of the melted sample at 72 °C and after cooling down to room temperature is similar to the not melted one, while the material shows high-temperature sustainability up to 180 °C. The EPR experiments confirm the tetrahedral environments of the Mn^{2+} ions. In this compound, the $[MnBr_4]_2$–tetrahedral units are isolated by large (TPA) organic cations, resulting in a unique 0D structure. This 0D perovskite emits a strong green light under UV excitation, with a maximum at 520 nm and a high photoluminescence quantum yield (PLQY) of 62% benefitting from the lowest d–d orbital transition of the Mn^{2+} ion in the tetrahedral crystal field and the long Mn–Mn distance, respectively. The photoluminescence lifetime of $(TPA)_2MnBr_4$ is 0.39 ms. Fluorescence lifetime imaging microscopy (FLIM) shows a uniform distribution of the emitting species with no apparent bulk or edge defects. A series of color-tunable down-converted light-emitting diodes (LEDs) were fabricated by using increasing amounts of $(TPA)_2MnBr_4$ as the phosphor layer, reflecting its high potential for application in LED technologies.

Introduction

During the last 2 decades, organic–inorganic hybrid lead (Pb) perovskites have attracted significant interest for their photoluminescence and electroluminescence properties such as large absorption coefficient, high charge carrier mobility, high photoluminescence quantum yield (PLQY), direct optical band gap and high defect tolerance.[1–10] However, the high toxicity of Pb-based materials and their poor stability remain the major

[a] Departamento de Química Física, Facultad de Ciencias Ambientales y Bioquímica, e INAMOL, Campus Tecnológico de Toledo, Universidad de Castilla-La Mancha (UCLM), Avenida Carlos III, S.N., 45071 Toledo, Spain. E-mail: abderrazak.douhal@uclm.es

[b] Engineering Laboratory of Organometallic, Molecular Materials, and Environment (LIMOME), Faculty of Sciences, Sidi Mohamed Ben Abdellah University, 30000 Fez, Morocco

[c] Departamento de Química Orgánica e Inorgánica, Facultad de Ciencia y Tecnología, Universidad del País Vasco, UPV/EHU, B Sarriena s/n, 48940 Leioa, Spain

obstacles to their practical application.[11,12] Therefore, an important way to overcome the toxicity issue is to replace Pb in perovskites with eco-friendly elements.[13,14] Compounds based on divalent Mn(II) cations have long been considered promising candidates to replace Pb^{2+} in organic–inorganic perovskites.[15,16] Manganese-based hybrid inorganic–organic materials have drawn significant attention not only in the fields of ferromagnetics[17–19] and solar cells,[20] but also for their good stability and high-performance emission with colors ranging from green to red depending on the coordination environment of Mn^{2+}.[21–24] The Mn^{2+} metal ion has a $3d^5$ electronic configuration and generally exhibits visible photoluminescence (PL) resulting from the $^4T_1$-$^6A_1$ transition,[25–27] which mainly depends on the crystal field surroundings of Mn^{2+} in the lattice. In some cases, the Mn^{2+} ions are tetrahedrally coordinated (weak crystal field), and each Mn^{2+} ion is surrounded by four ligands to form an independent $[MnX_4]^{2-}$ tetrahedral unit, where the Mn–Mn distance is large enough to eliminate direct spin–spin coupling between adjacent Mn ions.[28] In that case, the contributions from an individual Mn^{2+} ion dominate the optical transition, usually leading to green emission (500–550 nm) with a

286 | *J. Mater. Chem. C*, 2024, **12**, 286–295

This journal is © The Royal Society of Chemistry 2024

small full width at half maximum (FWHM) of 25–60 nm.[29–31] For other cases, when the Mn^{2+} ions are octahedrally coordinated (a strong crystal field), each Mn^{2+} ion is surrounded by six ligands ($[MnX_6]^{4-}$), and the Mn–Mn distance is largely reduced due to the formation of edge-sharing infinite linear chains along one direction. Therefore, the octahedral coordination of Mn^{2+} ions (higher Mn–Mn coupling interaction) induces a shift in the emission spectrum to orange or deep red spectral regions, with a large FWHM of more than 60 nm.[32–34] In some cases, it's has been found that the emission color of the Mn-based perovskites can be tuned from green to red during the phase transition from tetra-coordination to hexa-coordination of manganese(ɪɪ) ions.[35–37] Thus, Mn-hybrid perovskites show excellent gas sensing properties, X-ray scintillators, and good performance in terms of LEDs (light emitting diodes) with the advantages of low cost, environmental protection, and easy preparation.[23,38–42]
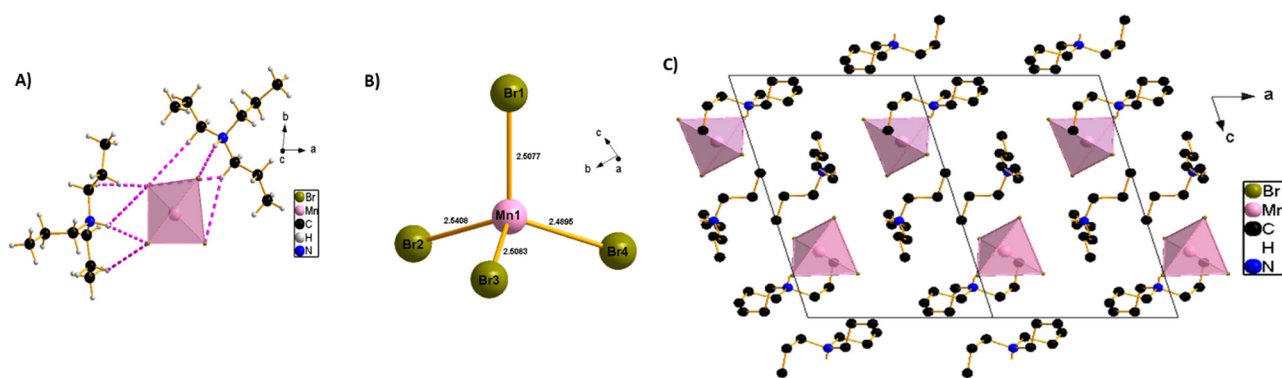
The organic ligand is an important structural component of the Mn-based perovskites that affects the electronic band structures and the corresponding crystal field. Organic cations with a rigid structure could reduce the thermal vibrations and suppress nonradiative transitions thus increasing the PLQY.[23] On the other hand, bulkier ligands in the correct molar ratio might allow tuning the optical properties of the resulting perovskites increasing the Mn–Mn separation. Although not as common, as an alternative strategy, smaller monovalent organic cations could also be used to obtain the required Mn–Mn distance to obtain highly efficient green-emitting Mn-based perovskites. Since they are monovalent, two such cations will be needed to charge balance the $[MnBr_4]^{2-}$ perovskite tetrahedra, which should lead to a longer separation between the Mn centers.[43] This approach has been used for example to produce green-emissive 0D Mn(ɪɪ)-based perovskite of formula $(LH)_2MnX_4$ (($TEM)_2MnBr_4$, TEM = triethylammonium) with a Mn–Mn distance of 8.85 Å and a PLQY of 50%.[44] Another study has reported $(DIPA)_2MnBr_4$ (DIPA = diisopropylammonium) perovskites, with a similar distance between the $[MnBr_4]^{2-}$ tetrahedron (8.85 Å) and a PLQY of 62.2%.[45] Thus, it can be expected that the stereochemistry of small monovalent cation (both the DIPA and TEM provide a significant degree of steric hindrance) plays a fundamental role in the optoelectronic properties of the formed Mn-based perovskites. Notably, these studies did not provide information on the stability of these materials against moisture under ambient conditions. Therefore, small monovalent cations of the ligands with increased steric hindrance, like the tri-n-propylammonium cation, for example, could be used to improve the PLQY of the green emissive Mn-based organic–inorganic halide materials and will help evaluate the impact of tertiary ammonium cations on the long-term stability of Mn-based metal halide perovskites.

Here, we prepared, characterized, and studied the spectroscopy and photodynamic properties of a new Mn(ɪɪ) based organic–inorganic hybrid perovskite material $(TPA)_2MnBr_4$ by using tri-n-propylammonium as the organic cation. The perovskite was obtained at a high yield using a slow evaporation method in two different solvents, with excellent reproducibility. It was fully characterized using a combination of single crystal X-ray diffraction (SCXRD), powder X-ray diffraction (PXRD), thermal analyses (TGA-DSC), electron-spin paramagnetic resonance (EPR), UV-Vis steady-state and time-resolved emission spectroscopy, and fluorescence confocal microscopy analyses. $(TPA)_2MnBr_4$ displays an intense green emission centered at 520 nm with a high quantum yield PLQY of 62% due to effective d–d transitions of tetrahedrally coordinated Mn^{2+}. Its emission decays monoexponentially with a lifetime of 0.39 ms. Furthermore, a series of down-converted LED devices were fabricated using the $(TPA)_2MnBr_4$ powder as a green phosphor deposited on a blue (465 nm) LED chip, showing the possibility of controlling the emission color of the device with the amount of the Mn-based perovskite. Therefore, our work shows that $(TPA)_2MnBr_4$ has great potential to be the next-generation of hybrid organic–inorganic Mn halides for LED technologies and may also present great opportunities for its use in other optoelectronic applications.

Experimental section

The Experimental section is described in detail in the ESI,† Section 1. It includes the synthesis procedure of tri-n-propylammonium bromide salt (TPA), and the corresponding

Scheme 1 (A) Crystal structure of $(TPA)_2MnBr_4$ in the asymmetric part of the unit cell, the pink dashed line shows the H-bonds between tri-n-propylammonium organic cations and $[MnBr_4]^{2-}$ tetrahedral units. (B) Mn–Br distances in the single $[MnBr_4]^{2-}$ tetrahedral units. (C) The packing diagram of $(TPA)_2MnBr_4$ viewed from the b-direction at room temperature; all the H-atoms had been omitted for clarity.

$(TPA)_2MnBr_4$ perovskite, both as a single crystal and as a crystalline powder (Fig. S1, ESI†). It also describes the fabrication of the LEDs and the techniques and experimental conditions used for the characterization of the perovskite.

Results and discussion

Structural characterization

The SCXRD experiment was carried out at 150 K and shows that the synthesized perovskite possesses a typical zero-dimensional crystal structure, with a chemical formula of $(TPA)_2MnBr_4$. It crystallizes in the triclinic phase and $P\bar{1}$ space group, with the lattice parameters of $a = 9.5444(2)$ Å, $b = 10.1056(2)$Å, $c = 15.1835(3)$ Å, $\alpha = 82.880(2)°$, $\beta = 73.734(2)°$, $\gamma = 83.119(2)°$ and $Z = 2$. The structure of a single unit of $(TPA)_2MnBr_4$ is shown in Scheme 1. Further details for the crystallographic parameters are provided in Tables S1–S3 (ESI†). The asymmetric unit of the compound (Scheme 1A) consists of two independent tri-n-propylammonium organic cations and one $[MnBr_4]^{2-}$ anion as the inorganic part. The Mn^{2+} metal cation has a tetrahedral geometry composed of four bromide ions to form $[MnBr_4]^{2-}$ anion units. The circumjacent space of $[MnBr_4]^{2-}$ is filled with tri-n-propylammonium organic cations via hydrogen (H) bonding in opposite directions, forming a unique 0D structure. The geometry of $[MnBr_4]^{2-}$ tetrahedrons can be regarded as a slightly distorted tetrahedral, with (Mn–Br) bond lengths varying from 2.5076(4) to 2.5408(4) Å, while the (Br–Mn–Br) angles vary from 106.654(14) to 109.781(14)° (Scheme 1B). These values of bond lengths and angles are in good agreement with those found in other reported $[MnBr_4]^{2-}$ tetrahedrons.[46–49] The crystal structure is stabilized by intermolecular H-bonding interactions between tri-n-propylammonium organic cations and $[MnBr_4]^{2-}$ complex anions via an intricate network of C–H···Br and N–H···Br H-bonds into a 3-dimensional network that stabilizes the resulting 0D perovskite (Scheme 1C and Table S3, ESI†). The Mn–Mn distances in $(TPA)_2MnBr_4$ (approximately 9.5444(5) and 10.0066(5) (longest) Å (Fig. S2, ESI†)) are sufficiently large to eliminate the direct spin–spin coupling between Mn-ions in independent $[MnBr_4]^{2-}$ tetrahedral units.[41] Hence, it is expected that its optical transition will be dominated by an independent manganese ion, resulting in a green emission.

Powder X-ray diffraction (PXRD)

The crystalline structure of the as-synthesized perovskite was confirmed via powder X-ray diffraction (PXRD) analysis (Fig. 1A). The PXRD pattern of $(TPA)_2MnBr_4$ is consistent with the simulated one obtained from the single crystal with slightly varying intensities (Fig. 1A), most probably due to preferential orientations, demonstrating the high phase purity and the uniformity of the synthesized crystals.

Hirshfeld surface analysis

To gain more insights into the nature and robustness of interactions present in the crystalline arrangements of $(TPA)_2MnBr_4$, Fig. S3A (ESI†) shows the Hirshfeld surfaces (HS) mapped using
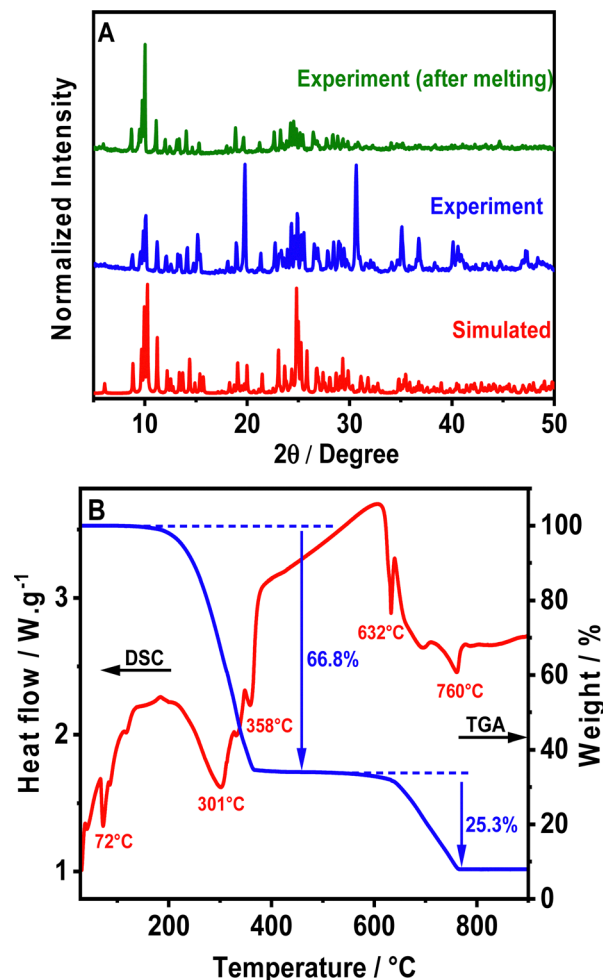

Fig. 1 (A) PXRD patterns of the powder sample of $(TPA)_2MnBr_4$, before and after melting, as well as the simulated PXRD pattern from SCXRD. (B) TGA-DSC curves of $(TPA)_2MnBr_4$.

d_{norm}. Clearly, the H–H intermolecular interactions provide the dominant contribution (69%) in the total surface of the molecular structure as it appears by the scattered points in the middle area of the fingerprint plot (Fig. S3B, ESI†). Furthermore, the H–Br/Br–H interactions, which appear as two pair sharp spikes in the fingerprint plot, have the second most dominant interaction contribution (30.7%). Due to the opposite partial electronic charge of the hydrogen and the bromine atoms, this kind of interaction is electrostatically favourable providing more robustness to the crystal. Notice that there are two different N–H···Br and C–H···Br H-bonds in the crystal structure (Fig. S3C and Table S3, ESI†) and the presence of these H-bonds exerts a large influence on the robustness of the packing in the crystalline arrangements. Finally, the Mn···Br intermolecular interaction (not within the same tetrahedron) is very weak, with only 0.3% contribution (Fig. S3D, ESI†).
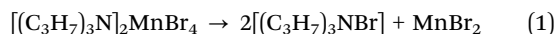
TGA-DSC analysis of the $(TPA)_2MnBr_4$ as-synthesized powder

Furthermore, we explored the thermal stability of $(TPA)_2MnBr_4$ through simultaneous thermogravimetric analysis (TGA) and

288 | *J. Mater. Chem. C*, 2024, **12**, 286–295

This journal is © The Royal Society of Chemistry 2024

differential scanning calorimetry (DSC) measurements from room temperature to 900 °C (Fig. 1B). The results show that the compound remains stable up to 180 °C and above this temperature it starts to decompose in two main weightless steps. In addition to that, a sharp endothermic peak in the DSC signal is observed at 72 °C, reflecting the melting of $(TPA)_2MnBr_4$ powder, but without any signature of decomposition since the material is still green emissive upon cooling down to room temperature (Fig. S1, ESI†). Notice also that the PXRD at room temperature of a melted sample (heated to 75 °C) is very similar to the not melted one (Fig. 1A). This indicates that even after melting, the $(TPA)_2MnBr_4$ perovskite retains its initial crystalline structure and maintains its green emission. This result is similar to the one reported for $(Bu_4N)_2[MnBr_4]$ (Bu_4N: tetrabutylammonium) in which the melting of the perovskite occurs at 60 °C.[50]

On the other hand, the first weight loss occurring between 220 and 400 °C, is attributed to the decomposition of two (TPA)-Br moieties. The observed weight loss in this step is 66.8%, very close to the theoretical mass expected for this ligand in the material (67.3%). This decomposition process is accompanied by two endothermic peaks on the DSC curve (red curve), with the maximum being at 301 °C and 358 °C, respectively. The thermal decomposition mechanism could take place according to the following eqn (1):

$$[(C_3H_7)_3N]_2MnBr_4 \rightarrow 2[(C_3H_7)_3NBr] + MnBr_2 \quad (1)$$

The last transformation between 400–780 °C, with a total weight loss of 25.3%, corresponds to the partial decomposition of the inorganic $MnBr_2$ unit. Subsequently, the residue is stable up to a temperature of 900 °C. These results agree with those observed for the thermal degradation of similar perovskites compounds.[49,51] For example, a systematic study of the thermal decomposition of Mn(II) perovskites with the general formula $(Et_4N)_2[MnBr_4]$ (Et_4N: tetraethylammonium cation) reveals that the decomposition of this perovskite leaves behind only a Mn(II) halide during the first step, which agrees well with our result.[52]

To further investigate the possibility of an order–disorder-type structural transition, DSC measurement of $(TPA)_2MnBr_4$ from 200 to 300 K (Fig. S4, ESI†) was carried out. However, surprisingly, no thermal signals were observed in the DSC curves during two cycles of heating and cooling, which confirms the absence of any phase transition or thermal anomalies in the prepared Mn perovskite.

EPR spectroscopy characterization

EPR spectroscopy is a useful tool to get important information about the local coordination of high-spin Mn^{2+} ions in all types of material.[53] Fig. 2A shows the X-band EPR spectra of powder samples of $(TPA)_2MnBr_4$ measured at different temperatures from 100 to 5 K, while Fig. S5 (ESI†) exhibits the X-band EPR spectra carried out at room temperature. The observed spectra are very complexes, with several broad lines from zero field to 0.7 T, indicating that the zero-field splitting (ZFS) in this compound is larger than the microwave quantum energy, $h\nu$, at this frequency.[54] Furthermore, the spectra do not change
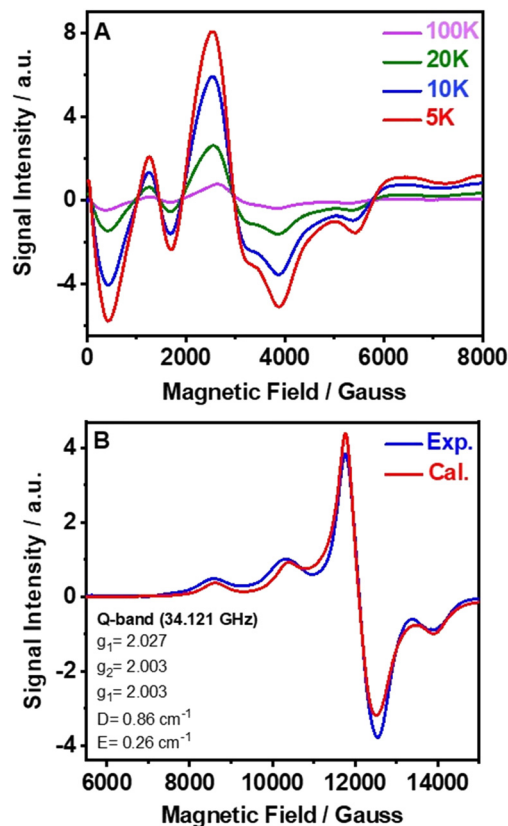

Fig. 2 (A) Variation of the X-band electron-spin paramagnetic resonance (EPR) spectra of $(TPA)_2MnBr_4$ with temperature from 5 to 100 K. (B) Experimental and calculated Q-band room temperature spectra (see the text for details of the fit).

significantly when the temperature is lowered to 5 K, which means that the ground state does not change and that the magnetic interactions between the Mn^{2+} ions are negligible. Notably, we did not observe the manganese nuclear hyperfine splitting. We explain this behavior by the presence of dipolar interactions in solid samples that lead to a broadening of the lines and as a result the hyperfine structure is often missing.[55]

The Q-band EPR spectrum recorded at room temperature has a much simpler appearance and a large signal intensity at $g = 2$ (Fig. 2B), indicating that the ZFS is smaller than the Zeeman energy at this frequency (34 GHz, 1.2 cm^{-1}). This spectrum could be reasonably well fitted using the following spin-Hamiltonian (eqn (2)):

$$\hat{H} = \beta B \cdot g \cdot \hat{S} + D\left[\hat{S}_Z^2 - \frac{S(S+1)}{3}\right] + E\left(\hat{S}_x^2 - \hat{S}_y^2\right) \quad (2)$$

where the first term accounts for the Zeeman effect, while D and E refer to the axial and rhombic parts of the ZFS, respectively. The spin Hamiltonian parameters were estimated by comparison of the experimental spectra with those obtained by a computer simulation program working at the second order of the perturbation theory (Bruker Symphonia software package). The parameters were then optimized using the least-squares method and the best-fit result is represented as a red solid line in Fig. 2B.

This journal is © The Royal Society of Chemistry 2024

J. Mater. Chem. C, 2024, **12**, 286–295 | **289**

The obtained ZFS constants are $D = 0.86$ cm^{-1} and $E = 0.26$ cm^{-1}, with g values close to 2 as expected for high-spin Mn(II) ions. Therefore, the Zeeman effect dominates the zero-field splitting in the Q-band experiments, but not in the X-band experiments, hence the large difference between the observed spectra. The obtained values of D and E imply a strong distortion of the Mn^{2+} environment in this compound.[56] This fact, the loss of the hyperfine structure, and the green emission color of the compound suggest a distorted tetrahedral geometry for (TPA)$_2$MnBr$_4$.

Photophysical characterization

To characterize the photophysical properties of (TPA)$_2$MnBr$_4$, we recorded the UV-vis absorption, excitation, and emission spectra (Fig. 3). As displayed in Fig. 3A, the diffuse reflectance (converted to Kubelka–Munk (KM) function) and the excitation spectra exhibit bands with multiple vibrational transitions in the UV and visible regions (G terms and D terms). In the UV region, the two most intense peaks are located at around 360 nm and 374 nm and correspond to the electronic transition from the $^6A_1$ (6S) ground state of Mn^{2+} to $^4E(D)$ and $^4T_2(D)$. On the other hand, the strong absorption bands at around 437 nm, 450 nm, and 467 nm (visible region) are attributed to the
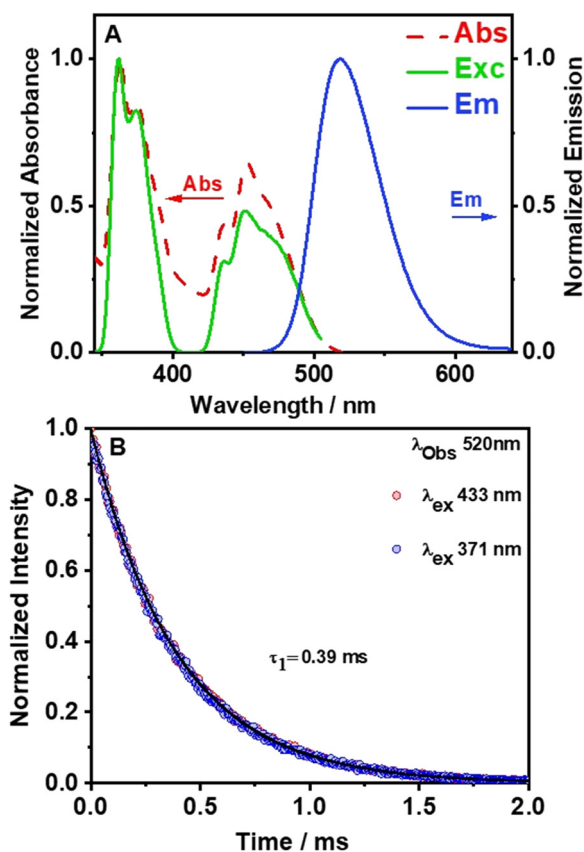

Fig. 3 (A) Normalized to the maximum intensity of reflectance (converted to the K–M function), excitation (observation at 520 nm), and emission (excitation at 365 nm) spectra of the (TPA)$_2$MnBr$_4$ as-synthesized powder. (B) Emission decays of the (TPA)$_2$MnBr$_4$ as-synthesized powder following excitation at 371 nm (blue circles) and 433 nm (red circles). The solid lines represent the best monoexponential fit.

transition of Mn^{2+} from the $^6A_1$ (6S) ground state to [$^4A_1(G)$, $^4E(G)$], $^4T_2(G)$, and $^4T_1(G)$ levels, respectively. Besides, the positions of these peaks are consistent with the energy state splitting for tetrahedrally coordinated Mn^{2+}.[49,57–59] The excitation spectrum of (TPA)$_2$MnBr$_4$ (monitored at 520 nm) matches well with the diffuse reflectance one indicating a common origin of the ground state transitions.

The emission spectrum of (TPA)$_2$MnBr$_4$ (Fig. 3A) was recorded upon excitation at the most intense absorption wavelength (365 nm). It consists of a single and relative narrow band (FWHM = 54 nm, 2127 cm^{-1}) with its maximum located at 520 nm (green color) and with a high PLQY of 62%. The strong green emission of this kind of Mn-perovskite is well known to be from the d–d ($^4T_1 \rightarrow {}^6A_1$) transition of Mn^{2+} ions with a tetrahedral coordination geometry in [MnBr$_4$]$^{2-}$ units. This is in agreement with the results from the SCXRD experiment where the long distance between two adjacent Mn^{2+} (approximately 9.54(5) (shortest) and 10.01(5) (longest) Å) reflects the absence of or weak Mn–Mn coupling in the [MnBr$_4$]$^{2-}$ tetrahedral units.[48,60,61] The tetrahedral units are separated enough by tri-n-propylammonium in the crystal structure leading to a Jahn–Teller effect, which induces the emission corresponding with the d–d transition of the Mn ions. Furthermore, the emission spectrum does not shift with the excitation wavelength (Fig. S6, ESI†), demonstrating that the emission of the perovskite material has its origin in the d–d transition of the Mn ions. Previous studies have shown that the Mn–Mn distance is a highly dominant factor for the PLQY in this kind of organic–inorganic compounds.[31,45,48,62] For example, in a systematic study of crystal structures and optical properties of several A$_m$MnBr$_4$-type perovskites (where m = 1 or 2, A = dimethylammonium, 3-methylpiperidinium, 3-aminomethylpiperidinium, heptamethylenimine, and trimethylphenylammonium) a direct correlation between the Mn–Mn distance and the PLQY was reported. The study demonstrated that higher PLQYs are associated with a longer Mn–Mn distance. The increase in the PLQY of these Mn-based compounds with the increase in the Mn–Mn distance was explained in terms of the reduction of the energy transfer processes (induced by coupling interactions such as dipole–dipole and spin–exchange interactions) between neighbouring Mn^{2+} ions.[43] Fig. S7A (ESI†), based on Table S4 (ESI†) shows that the PLQY of Mn(II)-based perovskites increases with the Mn–Mn distance as a result of inhibition of the Mn–Mn quenching by coupling effects, and thus, the emission is dominated by the d–d transition of each individual Mn ion. It was shown that a small enhancement of PLQY could occur also by other factors such as the type of the organic linker, the crystallinity of the synthesized single crystals and their symmetry and the degree of distortion in [MnBr$_4$]$^{2-}$.[48] The measured PLQY of 62%, which deviates from the ideal one (100%), suggests the presence of non-radiative processes that occur at shorter time scales.

As we previously discussed, the single crystal structure clearly shows the presence of H-bonds of CH$\cdots$Br (2.91 and 3.12 Å) and NH$\cdots$Br (2.36 and 2.39 Å). Thus, in addition to the weak Mn–Mn interaction and phonon (vibrations) channels for

the non-radiative deactivation, upon electronic excitation to $^4E(D)$, $^4T_2(D)$, $[^4A_1(G)$, $^4E(G)]$, $^4T_2(G)$, and $^4T_1(G)$ levels, the H-bond fluctuation in these states or in the emitting one, $^4T_1(G)$, should be an additional source for radiationless transitions which has been reported for many H-bonded systems.[63–65] Notice also that the presence of bromide atoms in the Mn-tetrahedral configuration could also induce radiationless transitions due to the heavy-atom effect in the emission transition.[66] Thus, we suggest that the weak Mn–Mn interaction, the H-bonds, the phonons, and the presence of bromide atoms around the Mn-emitter centre, all contribute to the decrease in the PLQY from 100% to 62%. Nevertheless, this is still a high value of PLQY, which encourages the use of this perovskite in lighting application as we will show in this contribution. Notice also that our experiments have been carried out at an ambient humidity of about 32%. Considering that the emission intensity in a down converter LED that was heated to 60 °C for 6 h increased by 13% (*vide infra*), we expect that the PLQY in a dry atmosphere should increase to at least 70–75%. Following Fig. S7 (ESI†) based on the published PLQY values of more than 30 tetrahedral Mn- and Br-based perovskites *vs.* Mn–Mn distance, the lowest expected value of the PLQY of our perovskite is about 50% while the highest one is about 90%.

To provide more insights into the photophysical properties of the hybrid Mn-perovskite $(TPA)_2MnBr_4$, the emission decay monitored at 520 nm was measured under two excitation wavelengths, 371 nm and 433 nm (Fig. 3B). The emission decay shows no dependency with either the observation wavelength nor the excitation one (Fig. S8, ESI†). The emission decays were accurately fitted using a single-exponential function with a time constant of 0.39 ms, indicating a single exciton recombination pathway. The long-lived emission lifetime value of this perovskite is due to the longer Mn–Mn distance (9.54 Å), which results in a lower energy transfer efficiency between Mn^{2+} emitting centres, suggesting that the d–d orbital transition dominated the emission lifetime. Table S4 (ESI†) shows that previously reported organic–inorganic manganese-based perovskites where the Mn emissive centre is in a tetrahedral configuration, exhibit an average lifetime in the microsecond time scale.

Using the value of the emission lifetime and PLQY, the calculated non-radiative rate constant (k_{nr}) is 0.97 s^{-1}. From the published PLQY and emission lifetime of tens of Mn(IV)- and Br-based perovskites (Table S4, ESI†), we calculated and plotted the change of k_{nr} *vs.* Mn–Mn shortest distance in the related single crystals (Fig. S7B and C, ESI†). The plot shows a significant dispersion of the data when considering all the data in Table S4 (ESI†). However, when the plot considers only the data for distances longer than 8.5 Å (Fig. S7D, ESI†), a clear trend is observed: a decrease in the k_{nr} value when the Mn–Mn distance increases. Notably, the Mn–Mn distance should be affected by the H-bond distances and forces of the CH···Br and NH···Br interactions (*vide supra*). Furthermore, an increase in the Mn–Mn distance will reduce the Mn···Mn coupling such as dipole–dipole and spin–exchange interactions between neighbouring Mn^{2+} centres. The value of k_{nr} obtained for
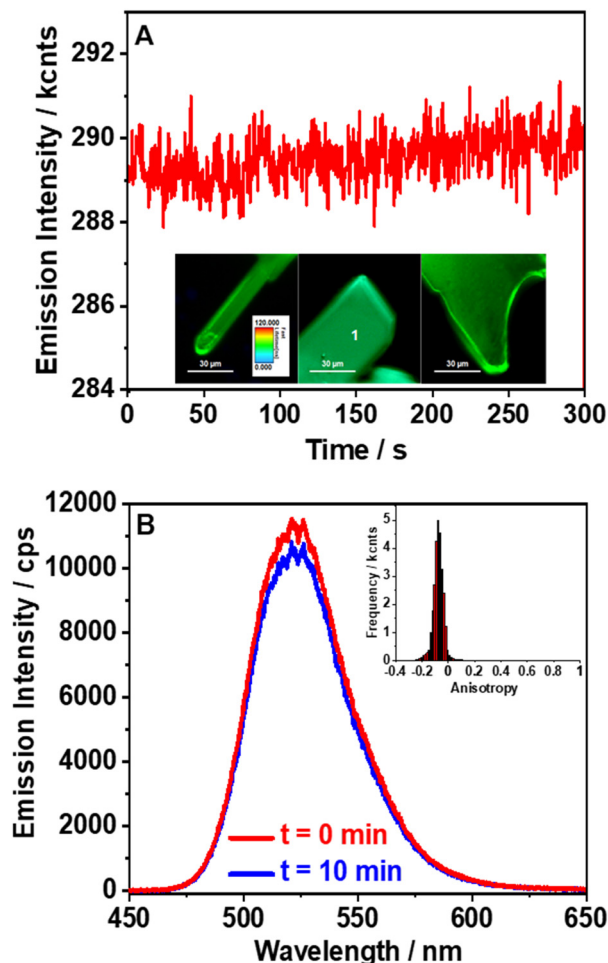

Fig. 4 (A) Long-term emission intensity stability collected at point 1 for 5 min constant laser irradiation (inset: fluorescence lifetime imaging microscopy (FLIM) images of a single $(TPA)_2MnBr_4$ crystal). (B) Emission spectra collected at point 1 before and after 10 min continuous laser irradiation (inset: anisotropy distribution histogram for the isolated crystal in Panel A). The excitation wavelength was 390 nm.

$(TPA)_2MnBr_4$ correlates well with the reported data for other Mn- and Br-based perovskites with similar Mn–Mn distances.

To further evaluate the properties of $(TPA)_2MnBr_4$, we also studied the fluorescence lifetime images (FLIM), stability, anisotropy distribution, and spectra of several individual crystals (Fig. 4). The FLIM shows a uniform distribution of the emitting species with no apparent bulk or edge defect contributions (inset of Fig. 4A and Fig. S9, ESI†). We also tested the stability of the emission intensity over a longer irradiation time. The recorded emission trace maintains the same intensity for 5 min under constant laser irradiation. Notably, we did not observe blinking behavior, which suggests that under these experimental conditions, there is no significant contribution from trap states or structural defects (Fig. 4A). Fluorescence blinking in perovskite crystals is often associated with trap states.[67] Therefore, the lack of blinking in the recorded emission traces indicates that no trap states are present in the studied crystals in agreement with the monoexponential

fluorescence lifetime behavior described above. The high stability is further confirmed by the emission spectra collected before and after 10 min of constant laser irradiation (Fig. 4B). Furthermore, the emission spectra collected in the bulk of the crystal and on its edges (Fig. S10, ESI†) show similar positions ($\sim$520 nm) and shapes with only small deviations in the intensity depending on the interrogated position. These spectra are also comparable to the steady-state emission one recorded for the powder samples, further supporting the homogeneous nature of this perovskite. Finally, we measured the anisotropy distribution of individual crystals. The obtained histograms are narrow and centred on values between −0.1 and 0 (inset of Fig. 4B and Fig. S11, ESI†). The narrow distribution agrees with the homogeneous nature of the crystals, while the value of the anisotropy suggests no preferential orientation of the emissive centres.

$(TPA)_2MnBr_4$ based down-converter LEDs

Next, based on the observed luminescence properties we employed $(TPA)_2MnBr_4$ for the construction of a series of down-converted LEDs. To this end, different amounts of $(TPA)_2MnBr_4$ were deposited on the surface of a blue (465 nm) LED chip (3.5 × 2.8 mm). Then, the 465 nm-LEDs were turned on to a voltage of 2.7 V (driving current of 18 mA), yielding different emission

colours in line with of the amount of $(TPA)_2MnBr_4$ used in the preparation of the devices (Fig. 5A). The emission spectra of the LEDs show a combination of two narrow bands with intensity maxima at 465 and 520 nm, corresponding to the emission of the blue LED chip and the Mn-perovskite, respectively (Fig. 5B). The increment in the amount of perovskite (from 4 to 10 mg) produce a progressive increase in the emission band intensity with a the maximum at 520 nm, enabling the control of the final colour by adjusting the amount of perovskite deposited onto the LED surface. In this sense, the final colour of the LEDs was modulated from light blue, with a CIE coordinate of (0.14, 0.16), to a greenish colour (0.17, 0.38), as depicted in Fig. 5C. Note that it is important to reach a compromise between the amount of material used to tune the emission color of the down-converted LED while maintaining its luminance. For this reason, we have not deposited larger amounts than 10 mg, since the emission of the LED was partially absorbed/blocked by the material, diminishing the emission of the device.

The photostability of the material was also tested during 9 hours of continuous operation (Fig. 5D). We realised that the material requires an activation period (irradiation by the blue LED) of 2 h before stabilization. During this time, the material does not suffer any photodegradation, but some fluctuations in the emission intensity were observed. In particular, it shows a
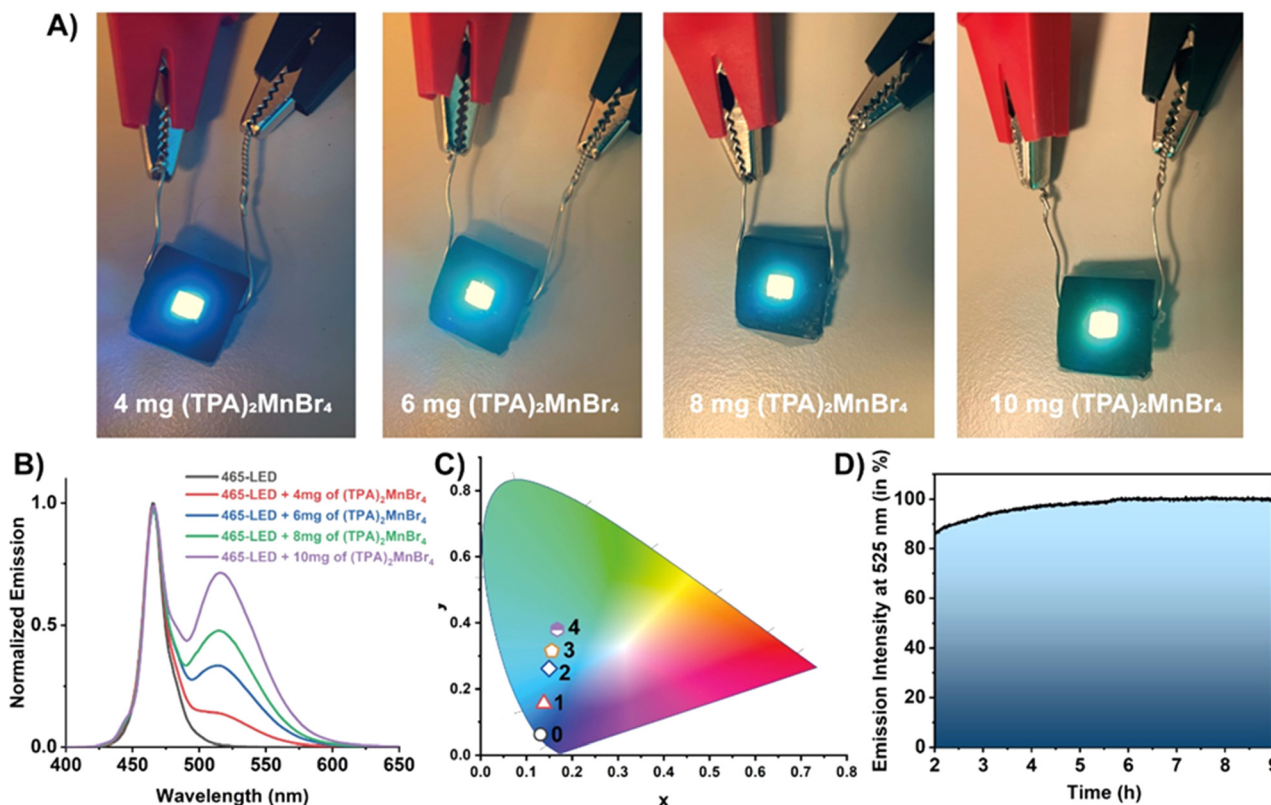

Fig. 5 (A) Real photos of the down-converted LEDs fabricated by depositing a certain amount of $(TPA)_2MnBr_4$ onto a blue 465 nm-LED chip. (B) Emission spectra of the LEDs under a driving current of 18 mA (2.7 V). (C) CIE chromaticity coordinates of the LEDs fabricated by coating a 465 nm blue LED with different amounts of $(TPA)_2MnBr_4$ perovskite: 0 = blue 465 nm LED; 1 = 4 mg; 2 = 6 mg; 3 = 8 mg and 4 = 10 mg of $(TPA)_2MnBr_4$. (D) Representation of the emission intensity collected at 520 nm (corresponding to the emission of $(TPA)_2MnBr_4$) of the LED prepared with 10 mg of $(TPA)_2MnBr_4$ under working operation conditions for a total of 9 hours.

292 | J. Mater. Chem. C, 2024, **12**, 286–295

This journal is © The Royal Society of Chemistry 2024

small fluctuation followed by an increase in the emission intensity. It is worth noting that the surface of this LED operating at 2.7 mV reaches a temperature of ~ 40 °C. In general, higher temperatures usually produce a quenching of the emission intensity due to an increase in the molecular vibrations promoting no radiave transitions. However, we observed the opposite effect when the material is deposited onto the LED surface. Since the presence of water molecules might partially reduce the crystallinity of $(TPA)_2MnBr_4$, it is possible that the presence of ambient moisture could diminish the emission intensity of this material. However, $(TPA)_2MnBr_4$ shows low sensitivity to moisture over time as evidenced by the PLQY measured after 45 days of storage under ambient conditions, which remained almost unchanged (61% vs. 62%). This also supports that water molecules, under ambient conditions, interacting with this perovskite do not affect significantly its photobehavior. In this sense, we propose that while the opto-electronic properties of the material are not significantly affected, heat released by the LED favours the detachment of moisture adsorbed on the surface of the Mn-perovskite powder, therefore, enhancing its emission until reaching a thermal equilibrium. Once the LED is warmed up and the equilibrium in the perovskite is established, the emission of $(TPA)_2MnBr_4$ remains almost constant (with a slight increase in the emission over the first 6 hours) as shown in Fig. 5D. This observation is of utmost importance because of two reasons: (i) the Mn-based perovskite material is highly photostable under these experimental conditions, in agreement with the results from FLIM; and (ii) for the fabrication of a possible commercial LED device, it would be critical to consider an appropriate balance between the water molecules and the heat release by the LED. To this end, it would be paramount to firstly activate the material (i.e., heating for removing the surface-attached water molecules) followed by coating of the LED under controlled experimental conditions and appropriate encapsulation of the down-converted LED device to avoid possible deterioration and therefore, to increase its useful lifetime. Hence, these results indicate the promising properties of $(TPA)_2MnBr_4$ perovskite for use as an active phosphor layer for the fabrication of colour tunable LED devices.

Conclusion

In summary, we synthesized a new organic–inorganic 0D-manganese-based perovskite $(TPA)_2MnBr_4$ using a slow evaporation method, with a triclinic phase and $P\bar{1}$ space group. The material exhibits high-temperature sustainability up to 180 °C, and the PXRD pattern after cooling down to room temperature of the melted sample at 72 °C is similar to the not melted one, indicating that the initial crystalline structure remains. $(TPA)_2MnBr_4$ displays an intense green emission centred at 520 nm with a high PLQY (62%), due to the effective d–d transitions of tetrahedrally coordinated Mn^{2+}. It also exhibits a lifetime of 0.39 ms. The FLIM images for $(TPA)_2$-$MnBr_4$ suggest a uniform distribution of the emitting species

with no apparent bulk or edge defect contribution. Moreover, green-light LED devices were prepared based on $(TPA)_2MnBr_4$ crystals. We belive that our results will contribute to the advancement on novel low-cost, high-performance, and eco-friendly organic–inorganic manganese-based perovskites as green-light-emitting devices in the future.

Conflicts of interest

The authors declare no conflicts of interest.

Acknowledgements

References

1 J. Sun, J. Wu, X. Tong, F. Lin, Y. Wang and Z. Wang, *Adv. Sci.*, 2018, **5**, 1700780.

2 Z. Wangen and D. Yang, *Small*, 2017, **13**, 1604153.

3 Q. Chen, N. De Marco, Y. Yang, T.-B. Song, C.-C. Chen, H. Zhao, Z. Hong, H. Zhou and Y. Yang, *Nano Today*, 2015, **10**, 355–396.

4 P. Xiao, Y. Yu, J. Cheng, Y. Chen, S. Yuan, J. Chen, J. Yuan and B. Liu, *Nanomaterials*, 2021, **11**, 103.

5 Z. Ma, Z. Shi, D. Yang, F. Zhang, S. Li, L. Wang, D. Wu, Y. Zhang, G. Na, L. Zhang, X. Li, Y. Zhang and C. Shan, *ACS Energy Lett.*, 2020, **5**, 385–394.

6 T. He, L. Saisai, Y. Jiang, C. Qin, M. Cui, L. Qiao, H. Xu, J. Yang, R. Long, H. Wang and M. Yuan, *Nat. Commun.*, 2020, **11**, 1672.

7 H. Peng, S. Yao, Y. Guo, R. Zhi, X. Wang, F. Ge, Y. Tian, J. Wang and B. Zou, *J. Phys. Chem. Lett.*, 2020, **11**, 4703–4710.

8 K. X. Steirer, P. Schulz, G. Teeter, V. Stevanovic, M. Yang, K. Zhu and J. J. Berry, *ACS Energy Lett.*, 2016, **1**, 360–366.

9 S. D. Stranks, G. E. Eperon, G. Grancini, C. Menelaou, M. J. Alcocer, T. Leijtens, L. M. Herz, A. Petrozza and H. J. Snaith, *Science*, 2013, **342**, 341–344.

10 G. Xing, N. Mathews, S. Sun, S. S. Lim, Y. M. Lam, M. Grätzel, S. Mhaisalkar and T. C. Sum, *Science*, 2013, **342**, 344–347.

11 W. Ning and F. Gao, *Adv. Mater.*, 2019, **31**, 1900326.

This journal is © The Royal Society of Chemistry 2024

J. Mater. Chem. C, 2024, **12**, 286–295 | 293

12 Q. Fan, G. V. Biesold-McGee, J. Ma, Q. Xu, S. Pan, J. Peng and Z. Lin, *Angew. Chem., Int. Ed.*, 2020, **59**, 1030–1046.

13 I. Lahbib, R. Mohamed and W. Sta, *J. Mol. Struct.*, 2016, **1120**, 250–258.

14 J. Huang, T. Chang, R. Zeng, J. Yan, Q. Wei, W. Zhou, S. Cao and B. Zou, *Adv. Opt. Mater.*, 2021, **9**, 2002267.

15 T. Huang, H. Penga, Q. Wei, C. Peng, Y. Tian, S. Yao, X. Han and B. Zou, *Nano Energy*, 2021, **93**, 106863.

16 X. Bai, H. Zhong, B. Chen, C. Chen, J. Han, R. Zeng and B. Zou, *J. Phys. Chem. C*, 2018, **122**, 3130–3137.

17 L. Septiany, D. Tulip, M. Chislov, J. Baas and G. R. Blake, *Inorg. Chem.*, 2021, **60**, 15151–15158.

18 S.-H. Park, I.-H. Oh, S. Park, Y. Park, J. H. Kim and Y.-D. Huh, *Dalton Trans.*, 2012, **41**, 1237–1242.

19 Y. Sozen, S. Özen and H. Sahin, *J. Magn. Magn. Mater.*, 2021, **531**, 167845.

20 Z. Nie, J. Yin, H. Zhou, N. Chai, B. Chen, Y. Zhang, K. Qu, G. Shen, H. Ma, Y. Li, J. Zhao and X. Zhang, *ACS Appl. Mater. Interfaces*, 2016, **8**, 28187–28193.

21 S. Balsamy, P. Natarajan, R. Vedalakshmi and S. Muralidharan, *Inorg. Chem.*, 2014, **53**, 6054–6059.

22 H.-Y. Ye, Q. Zhou, X. Niu, W.-Q. Liao, D.-W. Fu, Y. Zhang, Y.-M. You, J. Wang, Z.-N. Chen and R.-G. Xiong, *J. Am. Chem. Soc.*, 2015, **137**, 13148–13154.

23 D. Liang, H. Xiao, W. Cai, S. Lu, S. Zhao, Z. Zang and L. Xie, *Adv. Opt. Mater.*, 2023, **11**, 2202997.

24 L.-J. Xu, C.-Z. Sun, H. Xiao, Y. Wu and Z.-N. Chen, *Adv. Mater.*, 2017, **29**, 1605739.

25 Y. Zhang, W.-Q. Liao, D.-W. Fu, H.-Y. Ye, Z.-N. Chen and R.-G. Xiong, *J. Am. Chem. Soc.*, 2015, **137**, 4928–4931.

26 T. Zhuang, Y.-M. Lin, H.-W. Lin, Y.-L. Guo, Z.-W. Li, K. Du, Z. Wang and X.-Y. Huang, *Molecules*, 2023, **28**, 2380.

27 M. Li, J. Zhou, M. S. Molokeev, X. Jiang, Z. Lin, J. Zhao and Z. Xia, *Inorg.Chem.*, 2019, **58**, 13464–13470.

28 B. Su, G. Zhou, J. Huang, E. Song, A. Nag and Z. Xia, *Laser Photonics Rev.*, 2021, **15**, 2000334.

29 V. Morad, I. Cherniukh, L. Pöttschacher, Y. Shynkarenko, S. Yakunin and M. V. Kovalenko, *Chem. Mater.*, 2019, **31**, 10161–10169.

30 Y.-L. Wei, J. Jing, C. Shi, H.-Y. Ye, Z.-X. Wang and Y. Zhang, *Inorg. Chem. Front.*, 2018, **5**, 2615–2619.

31 H.-M. Pan, Q.-L. Yang, X.-X. Xing, J.-P. Li, F.-L. Meng, X. Zhang, P.-C. Xiao, C.-Y. Yue and X.-W. Lei, *Chem. Commun.*, 2021, **57**, 6907–6910.

32 Y. Zhang, W. Q. Liao, D. W. Fu, H. Y. Ye, C. M. Liu, Z. N. Chen and R. G. Xiong, *Adv. Mater.*, 2015, **27**, 3942–3946.

33 S. Wang, X. Han, T. Kou, Y. Zhou, Y. Liang, Z. Wu, J. Huang, T. Chang, C. Peng, Q. Wei and B. Zou, *J. Mater. Chem. C*, 2021, **9**, 4895–4902.

34 X.-F. Sun, P.-F. Li, W.-Q. Liao, Z. Wang, J. Gao, H.-Y. Ye and Y. Zhang, *Inorg. Chem.*, 2017, **56**, 12193–12198.

35 Y. Duan, Y. Ju, P. Xia, J. Qu, H. Shao, C. Wang, S. Xu and Y. Cui, *Opt. Mater.*, 2022, **134**, 113164.

36 K. Li, Y. Ye, W. Zhang, Y. Zhou, Y. Zhang, S. Lin, H. Lin, J. Ruan and C. Liu, *Nano Res.*, 2022, **15**, 9368–9376.

37 W. Gao, M. Leng, Z. Hu, J. Li, D. Li, H. Liu, L. Gao, G. Niu and J. Tang, *Dalton Trans.*, 2020, **49**, 5662–5668.

38 G. Zhou, Q. Ren, M. S. Molokeev, Y. Zhou, J. Zhang and X.-M. Zhang, *ACS Appl. Electron. Mater.*, 2021, **3**, 4144–4150.

39 B. Li, Y. Xu, X. Zhang, K. Han, J. Jin and Z. Xia, *Adv. Opt. Mater.*, 2022, **10**, 2102793.

40 W. Shao, X. Wang, Z. Zhang, J. Huang, Z. Han, S. Pi, Q. Xu, X. Zhang, X. Xia and H. Liang, *Adv. Opt. Mater.*, 2022, **10**, 2102282.

41 S. Yan, W. Tian, H. Chen, K. Tang, T. Lin, G. Zhong, L. Qiu, X. Pan and W. Wang, *Adv. Funct. Mater.*, 2021, **31**, 2100855.

42 S. Chen, J. Gao, J. Chang, Y. Zhang and L. Feng, *Sens. Actuators, B*, 2019, **297**, 126701.

43 L. Mao, P. Guo, S. Wang, A. K. Cheetham and R. Seshadri, *J. Am. Chem. Soc.*, 2020, **142**, 13582–13589.

44 M.-H. Jung, *Dalton Trans.*, 2023, **52**, 3855–3868.

45 C. Jiang, N. Zhong, C. Luo, H. Lin, Y. Zhang, H. Peng and C.-G. Duan, *Chem. Commun.*, 2017, **53**, 5954–5957.

46 N. O. Giltzau and M. Köckerling, *IUCrdata*, 2020, **5**, x200261.

47 L.-J. Xu, X. Lin, Q. He, M. Worku and B. Ma, *Nat. Commun.*, 2020, **11**, 4329.

48 N. N. Golovnev, M. A. Gerasimova, I. A. Ostapenko, A. O. Zolotov and M. S. Molokeev, *J. Mol. Struct.*, 2023, **1277**, 134851.

49 X.-W. Cai, Y.-Y. Zhao, H. Li, C.-P. Huang and Z. Zhou, *J. Mol. Struct.*, 2018, **1161**, 262–266.

50 A. Jana, S. Zhumagali, Q. Ba, A. S. Nissimagoudar and K. S. Kim, *J. Mater. Chem. A*, 2019, **7**, 26504–26512.

51 H. Fu, C. Jiang, J. Lao, C. Luo, H. Lin, H. Peng and C.-G. Duan, *CrystEngComm*, 2020, **22**, 1436–1441.

52 E. Styczeń, M. Gazda and D. Wyrzykowski, *Thermochim. Acta*, 2010, **503–504**, 21–27.

53 C. Duboc, *Chem. Soc. Rev.*, 2016, **45**, 5834–5847.

54 D. M. L. Goodgame, H. E. Mkami, G. M. Smith, J. P. Zhao and E. J. L. McInnes, *Dalton Trans.*, 2003, 34–35, DOI: **10.1039/B210407P**.

55 C. Duboc, M.-N. Collomb and F. Neese, *Appl. Magn. Reson.*, 2010, **37**, 229–245.

56 J. Krzystek, A. Ozarowski and J. Telser, *Coord. Chem. Rev.*, 2006, **250**, 2308–2324.

57 Y. Rodríguez-Lazcano, L. Nataf and F. Rodríguez, *Phys. Rev. B: Condens. Matter Mater. Phys.*, 2009, **80**, 085115.

58 T. Jiang, W. Ma, H. Zhang, Y. Tian, G. Lin, W. Xiao, X. yu, J. Qiu, X. Xu, Y. Yang and D. Ju, *Adv. Funct. Mater.*, 2021, **31**, 2009973.

59 W. Mao, J. Wang, X. Hu, B. Zhou, G. Zheng, S. Mo, S. Li, F. Long and Z. Zou, *J. Saudi Chem. Soc.*, 2020, **24**, 52–60.

60 Y. Cheng, H.-P. Ruan, Y. Peng, L. Li, Z. Xie, L. Liu, S. Zhang, H. Ye and Z.-B. Hu, *Chin. Chem. Lett.*, 2023, 108554.

61 H. Zhang, Y.-H. Tan, Y.-Z. Tang, X.-W. Fan, X.-L. Peng, R.-R. Han, Y.-K. Li and F.-X. Wang, *Inorg. Chem.*, 2022, **61**, 10454–10460.

62 S. Cao, C. Li, P. He, J. A. Lai, K. An, M. Zhou, P. Feng, M. Zhou and X. Tang, *ACS Appl. Opt. Mater.*, 2023, **1**, 623–632.

294 | *J. Mater. Chem. C*, 2024, **12**, 286–295

This journal is © The Royal Society of Chemistry 2024

63 A. Douhal, F. Lahmani and A. H. Zewail, *Chem. Phys.*, 1996, **207**, 477–498.

64 T. Elsässer and H. Becker, *Ultrafast hydrogen bonding dynamics and proton transfer processes in the condensed phase*, SSBM, 2013.

65 R. Ludwig, *ChemPhysChem*, 2007, **8**, 2539.

66 N. J. Turro, V. Ramamurthy and J. C. Scaiano, *Modern molecular photochemistry of organic molecules*, University Science Books Sausalito, CA, 2010.

67 M. D. Smith, B. A. Connor and H. I. Karunadasa, *Chem. Rev.*, 2019, **119**, 3104–3139.

This journal is © The Royal Society of Chemistry 2024

J. Mater. Chem. C, 2024, **12**, 286–295 | **295**